Effects of Freestream Acoustic Disturbances on Hypersonic Boundary Layer Stability

Geoffrey M. Andrews* and Jonathan Poggie.[†]
Purdue University, West Lafayette, IN, USA, 49707

Preliminary results are presented from an analysis of high-speed tunnel noise and its effect on hypersonic boundary layer transition. The acoustic noise profile of AEDC-VKF Tunnel B is approximated and used as an input to both linear stability and full Navier-Stokes calculations of a series of cone and hollow cylinder experiemnts. Apparent differences in the receptivity processes for these two canonical boundary layers are shown.

I. Nomenclature

T	=	Temperature
P	=	Pressure
α_r	=	Streamwise instability wavenumber
α_i	=	Streamwise instability growthrate
β_r	=	Spanwise instability wavenumber
β_i	=	Spanwise instability growthrate
ω	=	Instability angular frequency
f	=	Instability frequency
Re_x	=	Reynolds number based on streamwise distance
k	=	Disturbance wavenumber vector
ϕ_i	=	Disturbance phase constant
a_i	=	Disturbance amplitude

Subscripts

0	=	Stagnation conditions
1	=	Reference/normalization conditions

II. Introduction

THE topic of high-speed boundary layer transition is one of great importance to the development of a wide variety of hypersonic flight vehicles. The onset of turbulence in boundary layers has been observed to correspond to an sharp increase in heat flux and skin friction when compared to laminar flow, making the task of accurately predicting boundary layer transition one of significant relevance. Despite many decades of active research in the field, much of the underlying science of high-speed boundary layer transition remains poorly understood.

A topic of particular concern in the study of hypersonic boundary layers is the effect of the freestream disturbance environments in conventional high-speed wind tunnels on measurements of aerodynamic phenomena such as boundary layer transition. Early work by Kovasznay [1] characterized the fluctuating disturbances of turbulent flows into acoustic, entropic, and vortical fluctuations; Morkovin applied this framework to study the noise environment of conventional-design tunnels [2]. Key work on the topic was performed by Laufer, who recognised that turbulent boundary layers formed on the sidewalls of hypersonic tunnels radiate significant noise into the freestream environment of the test section [3, 4].

The effect of acoustic disturbances on hypersonic transition was specifically studied by Pate and Schueler [5], who compared measurements of transition on in nine different wind tunnels ranging from 30 cm to 130 cm in diameter. Their

---

*Ph.D. Candidate, School of Aeronautics and Astronautics, AIAA Student Member.
[†]Associate Professor, School of Aeronautics and Astronautics, AIAA Associate Fellow.

comparison showed that increased tunnel size led to two significant effects: decreased noise intensity, and increased transition Reynolds number. These observations supported the notion that freestream disturbances in conventional hypersonic tunnels is predominantly caused by acoustic radiation from turbulent boundary layers on the walls of the facility.

A similar study by Stainback [6] on a cone in six different hypersonic facilities at NASA Langley corroborated Pate and Schueler's observations on the importance of free-stream disturbances (specifically, pressure fluctuations resulting from turbulent boundary layers). Wind tunnel work by Kendall [7] elucidated details of the interactions between freestream facility noise and boundary layer instability, showing that the role of acoustic noise becomes increasingly significant as Mach number moves into the hypersonic regime. Extensive experimentation by Pate [8] using pairs of concentric shrouds to isolate test articles from freestream acoustic fields showed that for conventional hypersonic facilities, acoustic noise is a dominating factor in measurements of boundary layer transition. A comprehensive review of high-speed tunnel noise was published by Schneider [9], who summarized key studies of freestream noise in conventional ground facilities, ballistic ranges, and some flight experiments. A more recent study of wind tunnel data collected at eleven conventional hypersonic facilities by Marineau et al. [10] highlighted many of the trends reported by previous researchers, including a longstanding unit Reynolds number effect (initial amplitudes of boundary layer instabilities appear to scale with increasing unit Reynolds number) and a clear correlation between transition Reynolds number and tunnel size.

Facility noise has long been suspected to play a major role in the differing behavior of conical and planar boundary layers. Early work in the incompressible regime by Battin and Lin [11] and Tetervin [12] predicted that the ratio between conical and planar transition Reynolds numbers should be equal to 3. Experimental measurements, such as those by Potter and Whitfield [13] and Pate [14] produced a variety of values for this ratio, ranging from approximately 3 to 1 across a range of Mach numbers.

Pate surveyed the existing literature and, proposed a correlation for the conical-to-planar transition Reynolds number ratio as a function of turbulent skin friction coefficient along the tunnel wall [8]. This correlation showed remarkable qualitative agreement with data drawn from 11 different facilities, indicating that the ratio decreased monotonically with increasing Mach number from Mach 3 to 8.

However, the application of stability theory to the problem by Mack [15] suggests exactly the opposite of the available experimental data - that transition should occur later on flat plates than on cones due to lower disturbance growth rates in the flat plate case.

In order to address this discrepancy, Stetson et al. performed a series of experiments on a sharp cone and a sharp, hollow cylinder (used as a flat plate analog) at hypersonic speeds [16]. They collected detailed data on the growth of instabilities in each boundary layer but were not able to resolve the disagreement — their measurements were consistent with previous experimental data suggesting that cones have higher transition Reynolds numbers than plates. Notably, the data showed significant growth for low-frequency instabilities which was not predicted by LST. These results can be seen in plots of instability amplitude published in the the original paper, included below in Figure 1. These findings suggest that another instability mechanism may be dominant in the case of the hollow cylinder experiments; specifically, the unexpected growth of low-frequency waves is likely a result of low-frequency disturbances in the freestream. The authors posited that there may exist a fundamental difference in the receptivity of the two boundary layer categories such that for equivalent freestream disturbances, different instability waves are generated in the boundary layer of the cone versus the hollow cylinder.

Subsequent experiments conducted in quiet tunnels have corroborated this prediction. A significant work by Chen et al. [17] used NASA Langley's Pilot Low-Disturbance Tunnel (Mach 3.5), finding that the conical-to-planar transition Reynolds number ranged from 0.8 - 1.2 depending on unit Reynolds number. By running the tunnel with closed bleed valves, they generated high-noise conditions which led to a higher transition Reynolds number ratio; under low-noise conditions, the ratio dropped below 1. These values of transition Reynolds number ratio correspond well to predictions using linear stability theory, providing strong support for the theory that acoustic noise produced by turbulent sidewall boundary layers is a dominant factor in transition in conventional tunnels.

In recent years, the advent of direct numerical simulation (DNS) as an effective tool for scientific analysis has also been hugely beneficial for the study of hypersonic boundary layer transition; several experiments by Stetson et al. have been studied computationally. A 2003 paper by Zhong examined the receptivity of a blunt cone at Mach 8 to freestream disturbances [18], finding that second-mode waves are not directly excited by freestream disturbances, but instead arise due to resonance effects with excited first-mode waves. This synchronization between the first and second modes appears to play an important role in the receptivity of the boundary layer. Two works by Ma and Zhong performed a similar analysis on a flat plate at Mach 4.5, focusing on the resulting wave structures [19] and the freestream acoustic
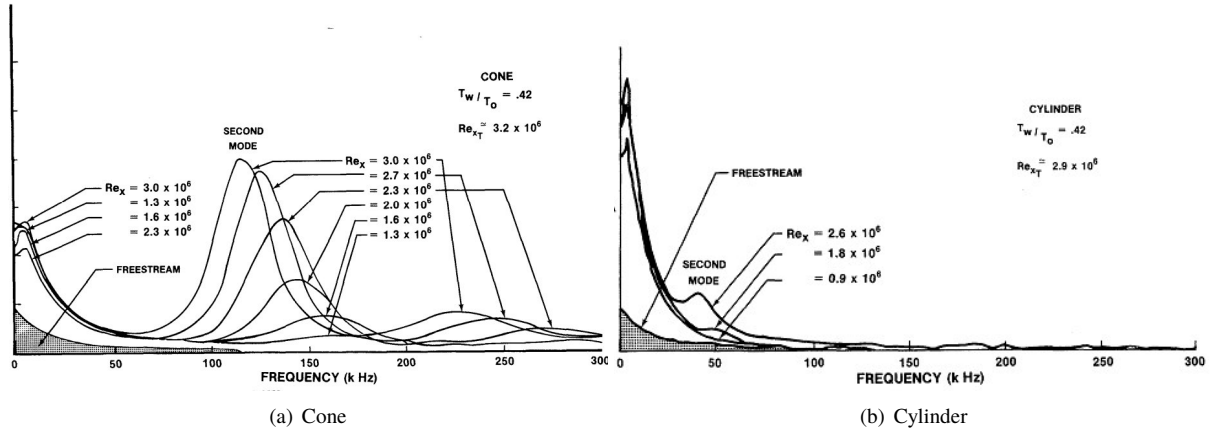
(a) Cone (b) Cylinder

Fig. 1 Instability amplitudes as a function of frequency from Stetson et al. [16].

disturbance receptivity process [20].

Another study by Balakumar [21] considered the receptivity of a flat plate boundary layer to acoustic disturbances, aiming to understand the relative importance of fast versus slow waves. The results show that slow waves more readily generated boundary layer instabilities due to the closeness in wavelength between the two waveforms. Work by Cerminara on a generic forebody shape [22] found very similar results; acoustic disturbances of the slow-wave form produced better agreement with experimental data, although they underpredicted the transition Reynolds number. This shortfall which may be attributable to inaccurate modeling of the wind tunnel noise environment, which highlights the need for accurate characterization of wind tunnel disturbance environments that can be grounded by comparison to experimental measurements.

The current work aims to study the cone and hollow cylinder experiments of Stetson et al. [16] to understand the effect of facility noise on measurements of hypersonic boundary layer transition. This paper demonstrates the use of linear stability theory (LST) and DNS to study the stability of boundary layers subject to acoustic radiation in a conventional hypersonic wind tunnel.

III. Experimental Geometry & Freestream Conditions

The experiments of Stetson et al. focused on two articles: a sharp cone and a hollow cylinder. The cone had an overall length of 1.016 m and a half angle of 7 degrees with a tip radius of 5.08×10^{-5} m. The cylinder (used as a flat plate analog to avoid three-dimensional end effects) had a length of 1.511 m, an outside diameter of 25.4 cm, and an internal diameter of 20.3 cm with the same specified tip radius of 5.08×10^{-5} m and a leading edge beveled at 15 degrees. Diagrams of the two models are shown below in Figures 2 and 3.
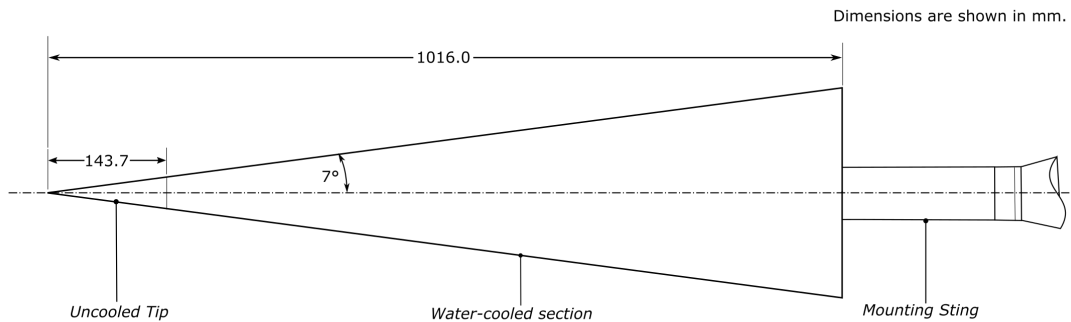

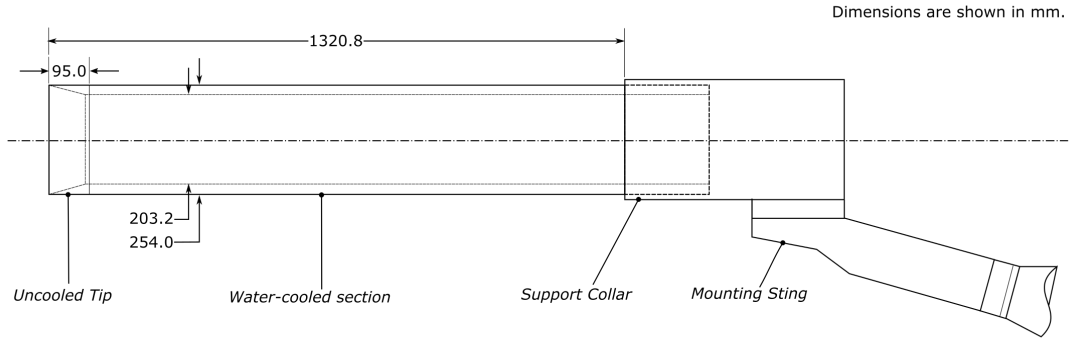**Fig. 2 Schematic of the cone of Stetson et al. [16].**

Fig. 3   Schematic of the cylinder of Stetson et al.[16].

Both models were made from concentric aluminium shells of approximately 3 mm thickness, between which cooling water circulated to maintain a constant surface temperature of 302 K. The tip regions of each article (14.4 cm for the cone and 9.5 cm for the cylinder) were fabricated from solid stainless steel. The effect of nose heating on transition was not addressed in detail by Stetson et al., but no change in transition location was observed with changes in the tip temperature over the course of experimental runs.

Stetson et al. performed their experiments in Tunnel B at the Arnold Engineering Development Complex von Karman Facility (AEDC-VKF). Tunnel B is a closed loop facility with a 1.27 m diameter test section and a range of available stagnation pressures from 345 kPa to 6.205 MPa. The air is vitiated using a natural gas heater to avoid condensation, while the tunnel surfaces itself are water-cooled. Different axisymmetric nozzles allow for operation at Mach 6 or Mach 8, with a unit Reynolds number range of 1.3×10^6 m^{-1} - 17.0×10^6 m^{-1}. Further details on the design and capabilities of Tunnel B can be found in Ref. [23]. The experiments of Stetson et al. were carried out using the Mach 8 nozzle and unit Reynolds numbers ranging from 3.2×10^6 m^{-1} to 6.4×10^6 m^{-1}. These flow parameters are summarised below in Table 1.

Mach Number	7.94
Velocity	1176.0 m/s
Static Pressure	165.5 Pa
Static Temperature	54.4 K
Unit Reynolds Number	3.2×10^6 m^{-1}
Model Wall Temperature	305.7 K

Table 1   Freestream conditions reported by Stetson et al. [16].

Due to the relatively long lifespan of AEDC-VKF Tunnel B, a large body of data characterizing its freestream environment is available. A 1995 study by Donaldson and Coulter [24] collated data from over 20 years of experiments in which hotwire anemometry was used to examine the noise environment of both tunnels. Data collected along the tunnel centerlines were processed to generate disturbance spectra for mass flux and total temperature fluctuations.

These results provide an idea of the relative amplitude of the freestream disturbances in each tunnel, up to a frequency of approximately 80 - 220 kHz (depending on unit Reynolds number), beyond which point the disturbances were indistinguishable from the instrumentation noise. Correlation between the instrumentation noise and the experimental measurements is an issue worth noting; as Schneider [9] observes, Donaldson and Coulter simply subtracted the "wind off" signal from the test measurements, which assumes that the instrumentation nose is completely uncorrelated with the measured variable.

For the purposes of replicating the AEDC Tunnel B environment computationally, the two spectra of normalized total temperature fluctuation provided by Donaldson et al. were used to interpolate a spectrum at $Re_x = 3.28 \times 10^6$ m^{-1} (corresponding to the experiments of Stetson et al. [16]), as shown below in Figure 4.
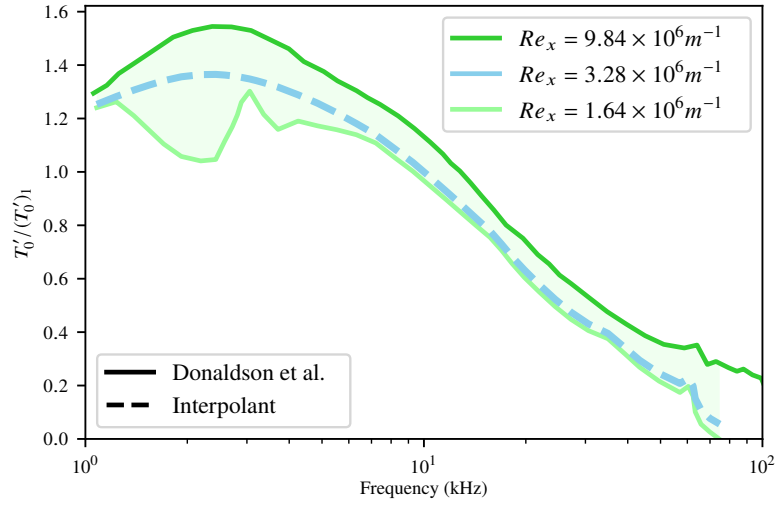
4

Fig. 4 Spectra of nondimensional total temperature fluctuations based on the work of Donaldon et al. [24].

The interpolated fluctuation spectrum shows good qualitative agreement with the freestream noise profile reported by Stetson et al. (see Figure 1(a)). Both profiles were scaled to provide unit area (i.e. divided by total signal energy so that the area under the curve is unity); a comparison of the two is shown below in Figure 5.
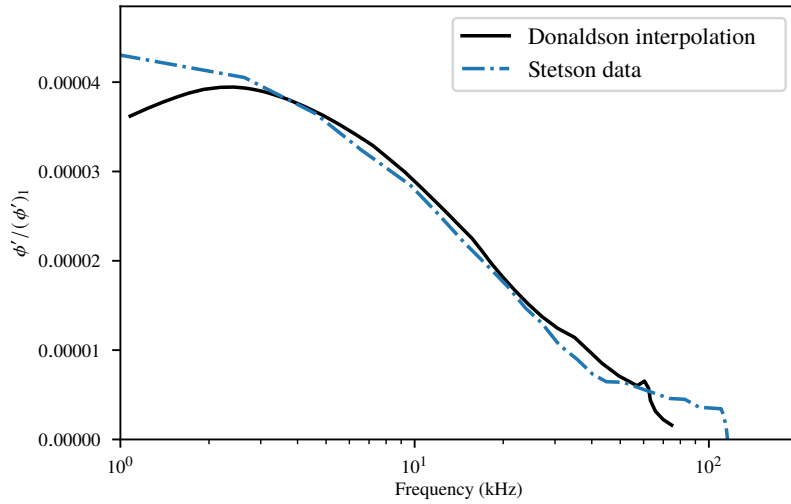

Fig. 5 Comparison of fluctuation spectra from Donaldson et al. [24] and Stetson et al. [16].

Marineau demonstrated that the spectral roll-off of freestream noise could be accurately modeled with a power law function; the power spectral density decreased in the range of frequencies corresponding to second mode frequencies with $f^{-3.5}$ [25]. In a 2019 survey paper by Duan et al. [26], this model was applied to measurements of freestream fluctuations in eleven different conventional hypersonic facilities (not including AEDC Tunnel B). A plot from this paper showing the power spectral density of normalized Pitot pressure fluctuations for five different facilities is copied below as Figure 6(a)). The power spectral densities of the scaled Donaldson interpolant and Stetson disturbance profiles are shown in comparison to this trendline in Figure 6(b).
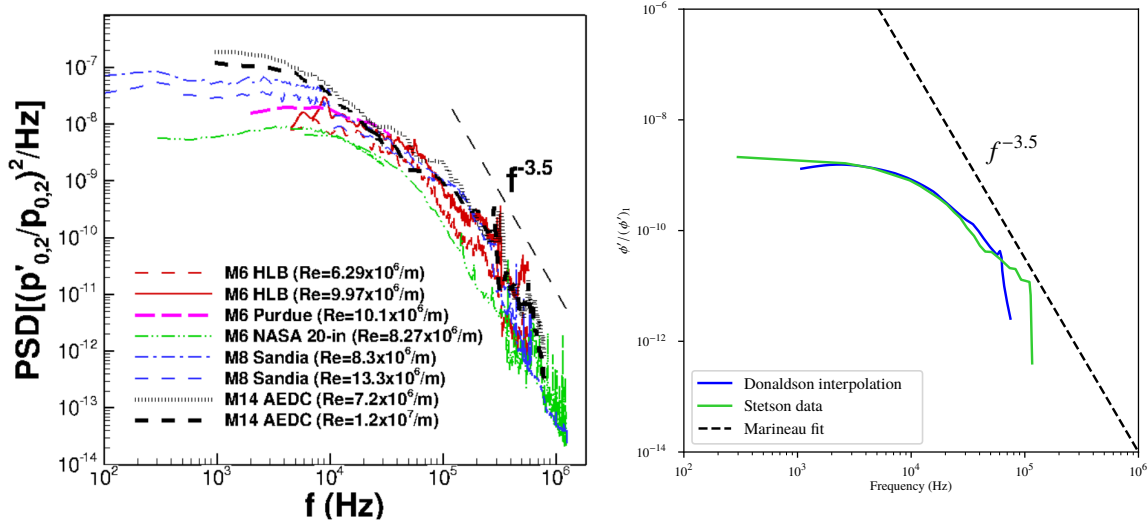
(a) Freestream pressure fluctuations of multiple facilities from Duan et al. (Fig. 2) [10]

(b) Fluctuations of Stetson et al. [16] and interpolant based on Donaldson et al. data [24]

Fig. 6   Freestream disturbance spectra.

While the data reported by Donaldson et al. [24] do not extend to frequencies high enough to show close agreement with the power law fit suggested by Marineau et al. [25], the available data show enough similarity with the available measurements from other facilities to suggest that the trend likely holds.

A piecewise curve was fit to the Donaldson interpolant, enabling calculation of an approximate fluctuation amplitude for an arbitrary frequency value.

$$\frac{T_0'}{(T_0')_1} = \begin{cases} 4.125 \times 10^{-5} \exp\left[-1.547 \times 10^{-1} \ln \left(f/3300\right)^2\right] & 0 \text{ kHz} \leq f \leq 11.6 \text{ kHz} \\ 1.530 \times 10^{-4} - 1.340 \times 10^{-5} \ln \left(f\right) & 11.6 \text{ kHz} \leq f \leq 90 \text{ kHz} \end{cases} \tag{1}$$

This function is shown plotted against the Donaldson interpolant in Figure 7; it shows near-exact agreement in the initial portion of the domain where the data indicate a curved distribution and close agreement in the steadily logarithmically-decreasing region thereafter.
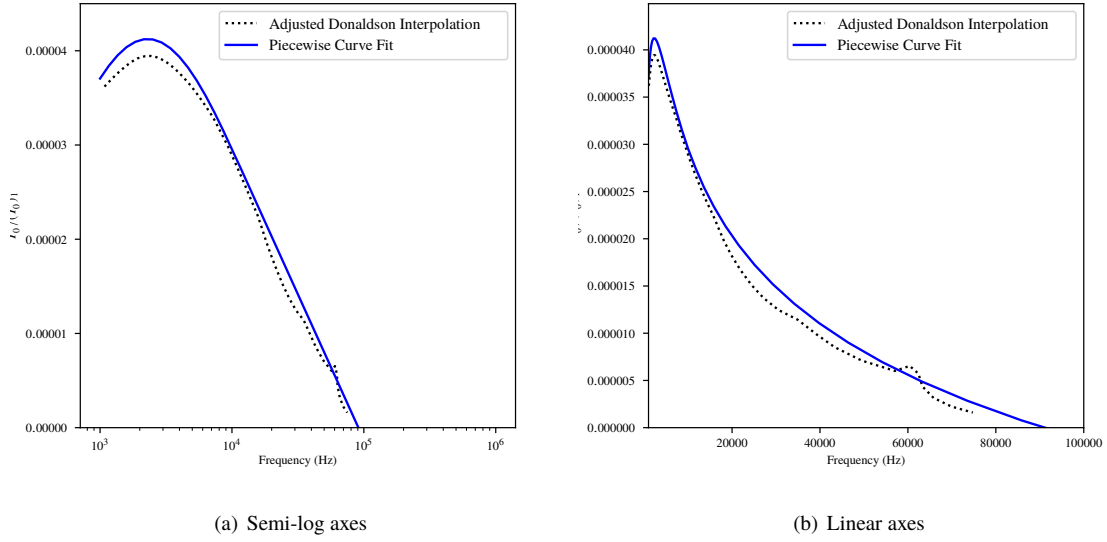
(a) Semi-log axes   (b) Linear axes

Fig. 7   Curve fit vs Donaldson interpolant.

IV. Linear Stability Theory

The application of linear and nonlinear stability theories is a well-known tool in the prediction of high-speed laminar-turbulent transition. Even in higher-fidelity analyses, the traditional stability theories provide a useful reference. Here, linear stability theory was applied to flow profiles generated by solving the boundary layer equations.

A. Governing Equations

The equations of linear stability theory are derived by writing flow quantities as the sum of an undisturbed laminar base flow and a fluctuating perturbation:

$$\phi = \bar{\phi} + \phi', \tag{2}$$

where $\bar{\phi}$ is the laminar flow quantity and ϕ' is the fluctuation. Substituting this form into the Navier Stokes equations and simplifying yields the LST equations, which can be solved to describe the behavior of the fluctuating flow properties (i.e. the instabilities). The equations have normal mode solutions of the following form:

$$\phi = \hat{\phi}(y)e^{i(\alpha x + \beta z - \omega t)}. \tag{3}$$

Here, ϕ' is a particular disturbance quantity (u_i', p', or T'), α and β are wavenumbers in the x and z directions, respectively, ω is the frequency, and $\hat{\phi}(y)$ is a function which provides the spatial structure of the disturbance in the y-direction. Whether the values of α, β, and ω are real or complex dictates the stability of the disturbance; if all are real then the disturbance is neutrally stable (i.e. it does not grow or decay in time or space); if α or β is complex, then the amplitude of the instability wave will change as it propagates through space (spatial instability); if ω is complex, then the amplitude of the instability wave will change with time (temporal instability). In general, temporal and spatial instabilities are not simply related as each harmonic component has a unique phase velocity, meaning that a group of instability waves of different frequencies will disperse as they propagate in time or in space.

When the linearized disturbance equations are discretized, they take the following form:

$$A\phi = f, \tag{4}$$

where ϕ is the solution vector containing the disturbance magnitudes for all points in the domain; f is a vector which encodes information about boundary conditions; and A is a matrix derived from the finite difference scheme. Solving the system for ϕ generates the eigenfunction for a specified β and ω. This solution — representing a particular instability mode — can then be tracked through the computational domain to analyze the amplification or attenuation of the disturbance as it progresses through the flow.

7

For this analysis, the VESTA code [27] was used to solve the equations of linear stability. The LST equations were treated as a spatial stability problem, in which one seeks a complex streamwise wave number $\alpha = \alpha_r + i\alpha_i$ corresponding to a specified instability frequency (ω) and spanwise wave number (β). In the VESTA code, the stability equations are solved using a Chebyshev collocation method. This approach allows for highly-accurate interpolation of the boundary layer profile while minimizing spurious oscillations at the domain boundaries (i.e. the Runge phenomenon) associated with other interpolant functions such as Lagrange polynomials [28].

High-quality boundary layer profiles were obtained by using the DEKAF solver [29] to solve the boundary layer equations for each axisymmetric geometry assuming a calorically perfect gas. The freestream conditions from the experiments of Stetson et al. as reported in Table 1 were used to generate these profiles, which are shown below in Figure 8; they have the expected self-similar shape and the development of the flow is evident from comparison of progressive streamwise locations.
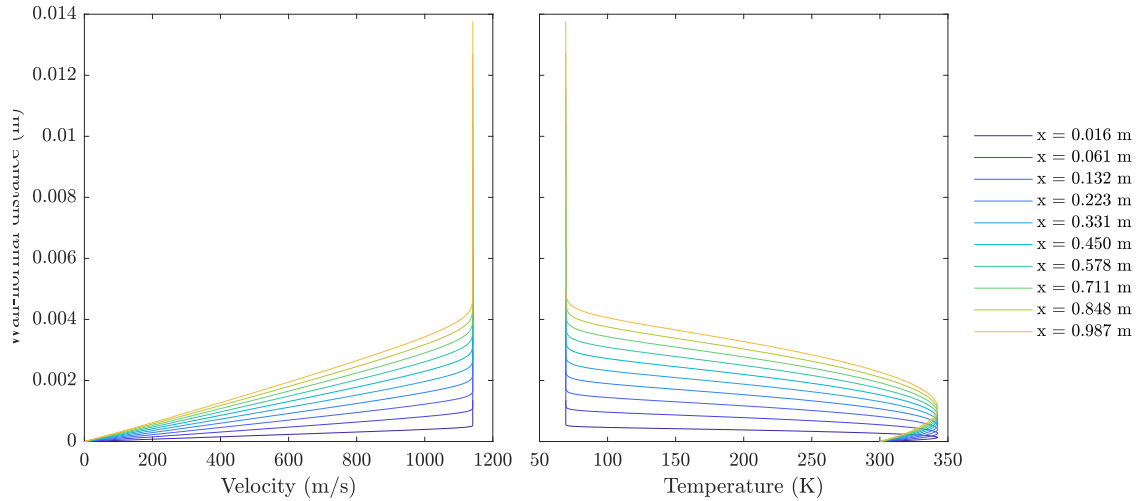
(a) Cone
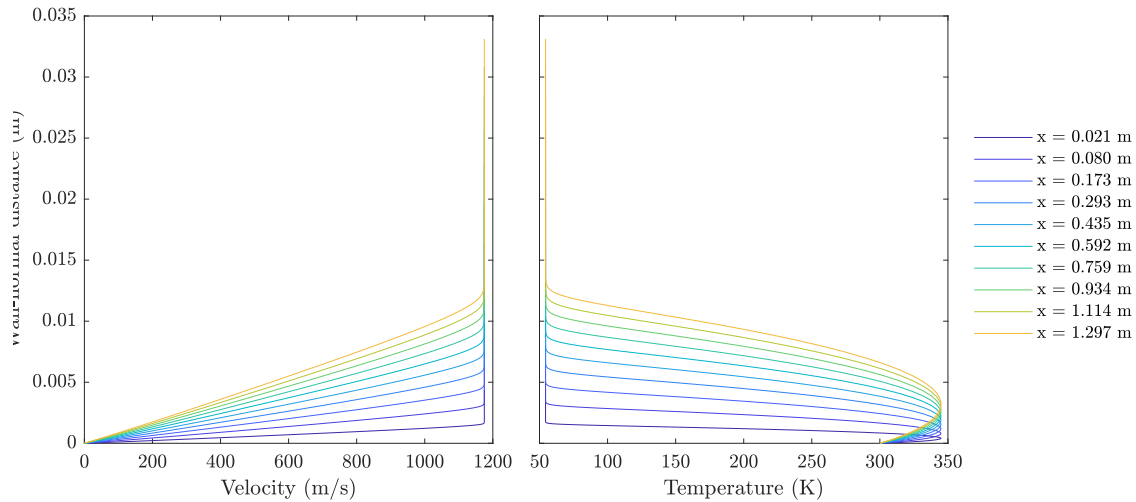
(b) Cylinder

Fig. 8 Boundary layer profiles generated by DEKAF solver at $Re_x = 3.28 \times 10^6$ m^{-1}.

Since the boundary layer equations are implicitly limited by their omission of higher-order terms from the Navier-Stokes equations, it is important to verify that the profiles obtained numerically are an adequate match for the experiments of Stetson et al. [16]. The results are roughly comparable to the experimenally-measured profiles, as seen in Figure 9, which shows both results for a series of Reynolds numbers based on streamwise distance. At increasing

Reynolds numbers (i.e. further downstream locations) for each flow, the agreement deteriorates; this is explained by the experimental boundary layers' evolution from laminar to transitional. In their paper, the authors also note that the boundary layer profiles obtained in their experiments are not of high quality, as the Pitot pressure probe experienced significant interference in the vicinity of the models' surfaces [16]. In light of this, the self-similar solutions obtained from the boundary layer equations would appear adequate for an initial linear stability analysis.
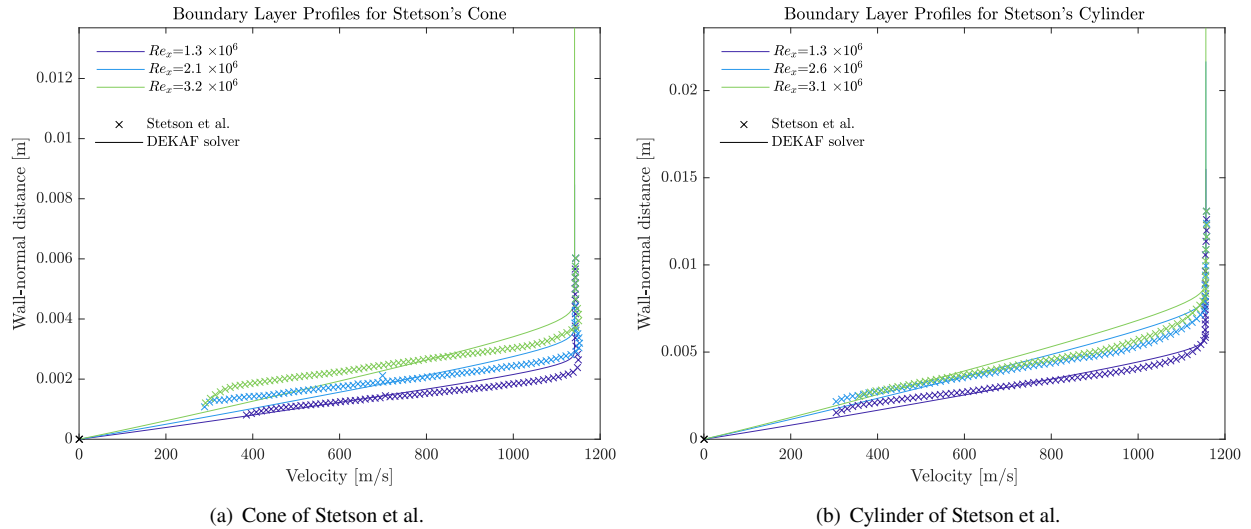

(a) Cone of Stetson et al.   (b) Cylinder of Stetson et al.

Fig. 9 Computed boundary layer profiles vs. experimental data of Stetson et al. [16].

The equations of linear stability theory have been solved for each of the boundary layers generated by DEKAF using the VESTA code. Boundary layer profiles for each flow were read into the code and used to perform a global eigenvalue search, providing a complete picture of the instability modes that exist in the linear regime (i.e. excluding modes that vanish under the assumption of locally parallel flow such as Görtler vortices). Within the spectrum of eigenvalues, specific instability modes can be selected by examining the eigenfunctions of their disturbances; these modes can then be followed using a local eigenvalue search to understand their stability at different points in the spatial and frequency domains.

Figure 10 shows curves of neutral stability for the cylinder and cone geometries; each curve represents the locus of points for which the amplification rate $-\alpha_i$ is 0, indicating a disturbance of neutral stability (i.e. one that is neither amplified or attenuated). Points on the interior of these curves represent unstable perturbations, while the exterior points correspond to stable perturbations.
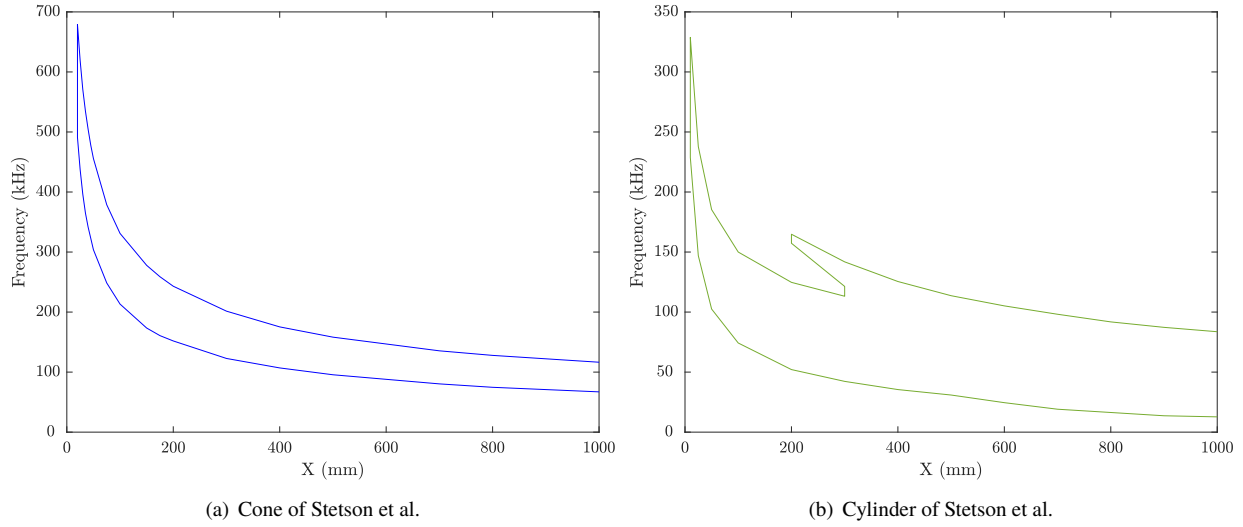
(a) Cone of Stetson et al.

(b) Cylinder of Stetson et al.

Fig. 10   Neutral curves generated from LST calculations.

For the cone, the neutral curve shows that instabilities of less than approximately 70 kHz are stable throughout the domain; a wide band of instabilities between approximately 70 kHz and 200 kHz are amplified through most of the domain; frequencies above 200 kHz are strongly amplified near the nose but damped elsewhere.

The behaviour of the cylinder is broadly similar, with a band of stable frequencies at the very low end of the spectrum (less than 10 kHz), a broad range of amplified frequencies (approximately 10 kHz to 130 kHz), and a range of higher frequencies amplified near the nose. However, the neutral curve for the cylinder displays a more complex disturbance spectrum consisting of higher modes, as seen in the multivalued top surface of the curve.
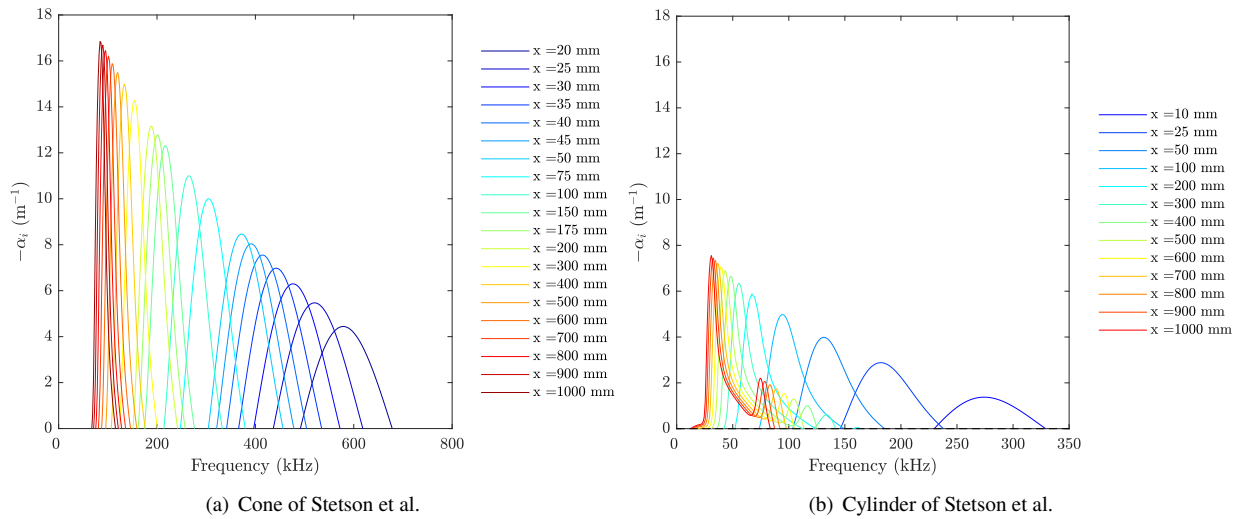

(a) Cone of Stetson et al.

(b) Cylinder of Stetson et al.

Fig. 11   Amplification rates at various downstream distances.

The additional mode which appears in the cylinder disturbance spectrum is clearer in the plots of amplification rate shown in Figure 11. Plot (a) shows amplification rates for the cone; these curves represent second-mode disturbances across the same band of frequencies covered by the neutral curve. Lower frequencies experience the strongest amplification in the downstream region; higher frequencies are weakly amplified near the nose and damped thereafter.

The curves in (b) show the harmonic behaviour of the second mode for the cylinder; each has a characteristic twin peak shape which becomes progressively stretched out as the disturbance propagates downstream. The two peaks create

10

multiple regions of instability, leading to the peculiar shape of the neutral curve. Another salient feature, not obvious from the neutral curves, is that the amplification rates for the cylinder are much lower than those for the cone - the second mode has both a lower frequency range and a lower rate of amplification in the cylindrical boundary layer versus the conical boundary layer.
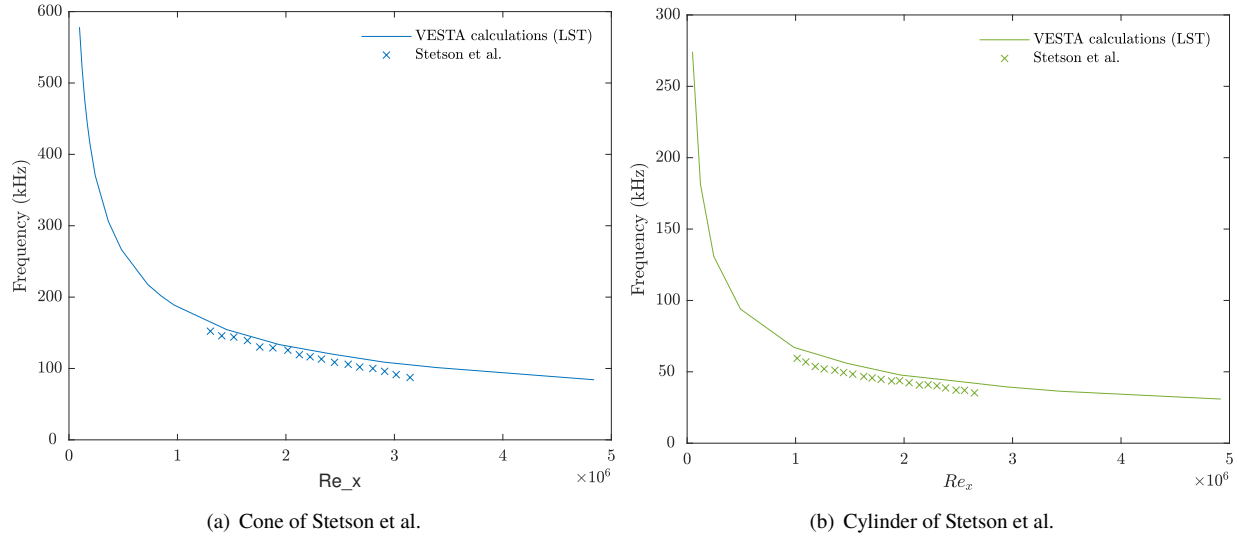

(a) Cone of Stetson et al.

(b) Cylinder of Stetson et al.

Fig. 12 Frequencies of maximum second-mode growth computed via LST vs data of Stetson et al. [16].

In both sets of amplification rate curves, the first mode appears stable as expected from the experiments of Stetson et al. [16]. In addition, the maximum growth rates correspond well with the experimental data; this is shown in Figure 12. The wind tunnel data show an approximately linear relationship between the maximally unstable frequency and the streamwise Reynolds number for both the cone and the cylinder, but the LST analysis suggests that the experiments simply failed to capture upstream behaviour of the second mode.

Calculation of the amplification factor $-\alpha_i$ of a frequency across a range of streamwise locations makes it possible to study the growth of an instability as it propagates downstream, as is done in the e^N method of transition prediction [30, 31]. This makes it possible to calculate instability spectra like those published by Stetson et al. [16] (reproduced above in Figure 1). Assuming that there are initially no significant instabilities in the boundary layer, the result is an estimate of the boundary layer stability when the receptivity is zero (i.e. freestream disturbances do not generate any initial instabilities within the boundary layer). These results are shown below in Figure 13.
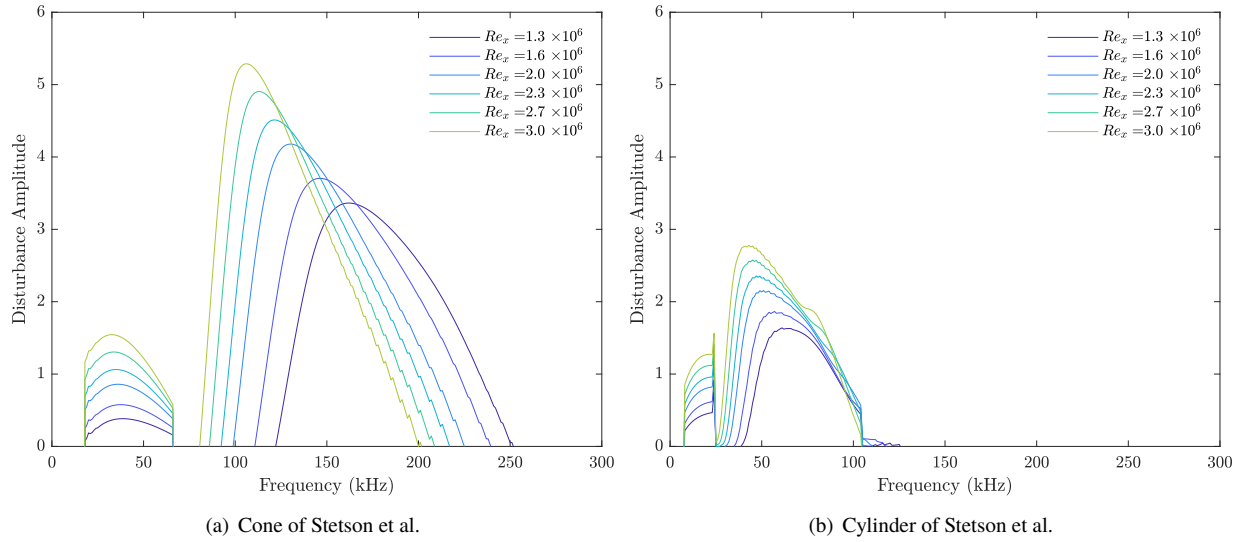
(a) Cone of Stetson et al.

(b) Cylinder of Stetson et al.

Fig. 13 Growth of disturbance amplitudes with increasing streamwise Reynolds number.

Conversely, Equation 1 can be used to generate initial amplitudes for the instability spectrum based on the tunnel noise profile assuming perfect receptivity - i.e. tunnel noise directly generates initial boundary layer instabilities with no modulation or attenuation. These results are shown in Figure 14.
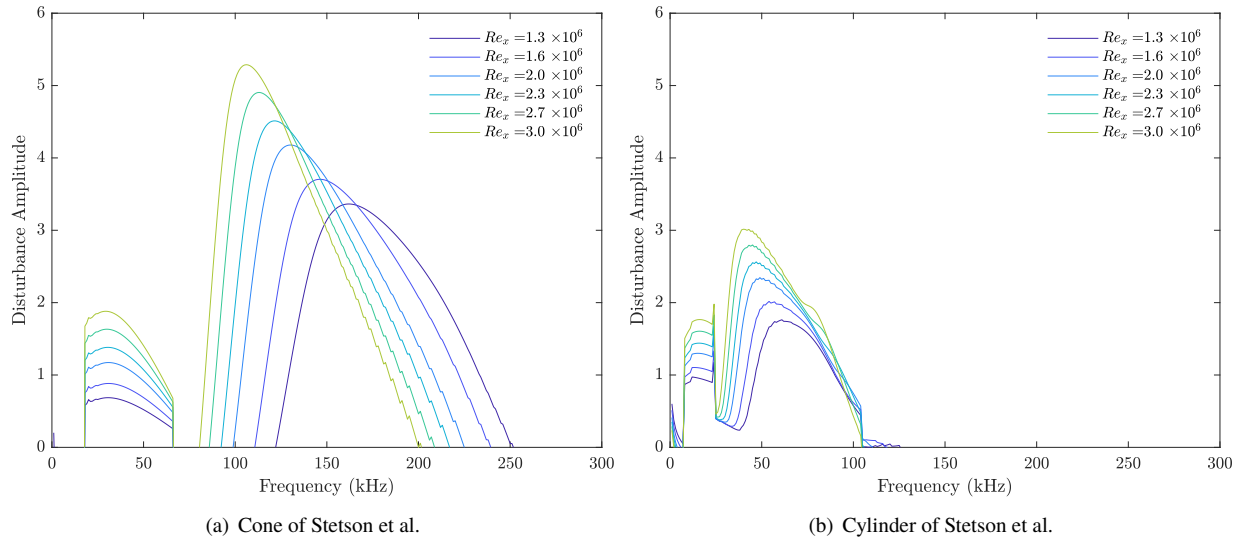

(a) Cone of Stetson et al.

(b) Cylinder of Stetson et al.

Fig. 14 Growth of disturbance amplitudes with increasing streamwise Reynolds number.

Comparison of these figures indicates that for this simplified analysis, LST does indeed predict modest growth of the low-frequency disturbances reported by Stetson et al. However, the growth only appears in the cylindrical boundary layer and is much lower in amplitude than seen in the instability spectra of Stetson et al. (Figure 1). This suggests that the receptivity of the cylindrical (i.e. planar) boundary layer to low-frequency freestream disturbances is indeed much higher than that of the conical boundary layer, but the mechanism is not well captured by straightforward LST.

12

V. Direct Numerical Simulation

An initial study of boundary layer receptivity to freestream noise has been undertaken by simulating the experiments of Stetson et al. [16] with an acoustic body force source term in the freestream. This simulates the acoustic disturbances generated by turbulent boundary layers on the sidewalls of AEDC-VKF Tunnel B.

A. Governing Equations

The physics of the hypersonic flow studied in these computations were modeled using the Navier-Stokes equations for an ideal, compressible gas. The conservation equations were tranformed from Cartesian coordinates (i.e. x, y, z) to the coordinates of the computational grid (ξ, η, ξ). In nondimensional form, the equations can thus be expressed in terms of vectors:

$$\frac{\partial \bar{U}}{\partial t} + \frac{\partial \bar{F}_j}{\partial \xi_j} = \frac{\partial \bar{G}_j}{\partial \xi_j} + \bar{S} \tag{5}$$

where the solution vector U and flux vector F_i are defined as

$$U = \begin{bmatrix} \rho \\ \rho u_1 \\ \rho u_2 \\ \rho u_3 \\ E \end{bmatrix} \tag{6}$$

$$F_1 = \begin{bmatrix} \rho u_1 \\ \rho u_1 u_1 + p \\ \rho u_1 u_2 \\ \rho u_1 u_3 \\ \rho u_1 (E + \frac{p}{\rho}) \end{bmatrix}, F_2 = \begin{bmatrix} \rho u_2 \\ \rho u_1 u_2 \\ \rho u_2 u_2 + p \\ \rho u_2 u_3 \\ \rho u_2 (E + \frac{p}{\rho}) \end{bmatrix}, F_3 = \begin{bmatrix} \rho u_3 \\ \rho u_1 u_3 \\ \rho u_2 u_3 \\ \rho u_3 u_3 + p \\ \rho u_3 (E + \frac{p}{\rho}) \end{bmatrix}, \tag{7}$$

and the transformed solution vector $\bar{U}$ and flux vectors $\bar{G}_i$ are defined in terms of the grid transformation Jacobian, J and the grid metrics as:

$$\bar{U} = \frac{U}{J} \tag{8}$$

$$\bar{G}_i = \left(\frac{\partial \xi_i}{\partial x_j} \right) \frac{G_j}{J}. \tag{9}$$

The governing equations were solved using the Wabash code (formerly Higher Order Plasma Solver, or HOPS) developed by Poggie [32–36]. This code uses a compact differencing scheme for spatial discretization which is sixth-order at interior points and fourth-order at boundaries with a reduction to a second-order upwind scheme near shocks. Temporal discretization uses an implicit method similar to the Beam-Warming scheme [37]; this results in a tridiagonal system of equations which is then solved using the approximate-factorization algorithm of Pulliam and Chaussee [38]. This discretization provides second-order accuracy in time.

To ensure the stability of the numerical scheme, a high-order filtering algorithm was implemented. The filter serves a purpose analogous to that of artificial damping; i.e. smoothing out the solution and limiting the growth of numerical instabilities. A low-pass, non-dispersive Padé-type filter is applied after each time step; the filter has an implicit form based on a local average of ϕ and neighboring values of $\bar{\phi}$. A more detailed description of the filter can be found in references [39] and [40].

B. Forcing Formulation

The method used for the freestream forcing is a superposition of random plane waves, similar to techniques demonstrated by Cerminara et al. [22] and Tufts et al. [41]. A number of discrete waves within a specified frequency spectrum are input to the code as a body force source term in the Navier-Stokes equations of the following form:

$$\vec{f} = A \sum_i a_i cos \left(\frac{\omega_i \vec{x} \cdot \hat{n}}{|a + V n_1|} - \omega_i t + \phi_i \right) \tag{10}$$

where ω_i and ϕ_i are the angular frequency and phase constant, respectively; a and V are the wave speed and local flow velocity, a_i is an amplitude constant, and $\hat{n} = \vec{k}/|\vec{k}|$ is the unit vector in the direction of the wave. The wave direction vector is $n = \langle \cos\theta_1, \sin\theta_1 \cos\theta_2, \theta_1 \sin\theta_2 \rangle$.

The forcing is implemented by selecting $i = 100$ modes evenly spaced across a frequency range spanning 10 kHz - 100 MHz with phase constant ϕ_i and wave direction angles θ_1, θ_2 generated randomly for each. The frequency range is based on the freestream disturbance spectrum of AEDC Tunnel B as reported by Stetson et al. [16] (Figure 1); the amplitude distribution $a_i(\omega_i)$ is generated from a curvefit.

VI. Results of Freestream Body Forcing

The governing equations were solved for both the cone and cylinder using dense structured grids of 1.3 billion cells, sufficient to capture the entire surface of each test article. With the forcing formulation given by Eq. 10 applied to a region ahead of the shock structure generated by each geometry, the manner in which these disturbances are processed by the shock and the boundary layer can be observed. While detailed analysis of these data is forthcoming, the initial results are shown in Figures 15 and 16.
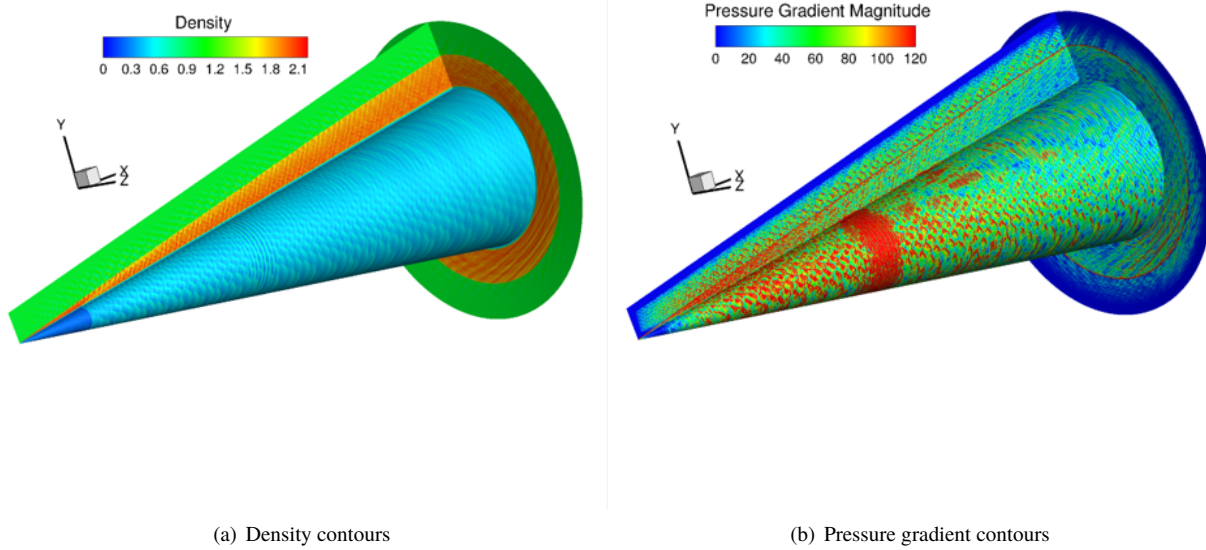

(a) Density contours

(b) Pressure gradient contours

Fig. 15   Simulation of Stetson et al. [16]'s cone subject to freestream acoustic forcing.

(a) Density contours
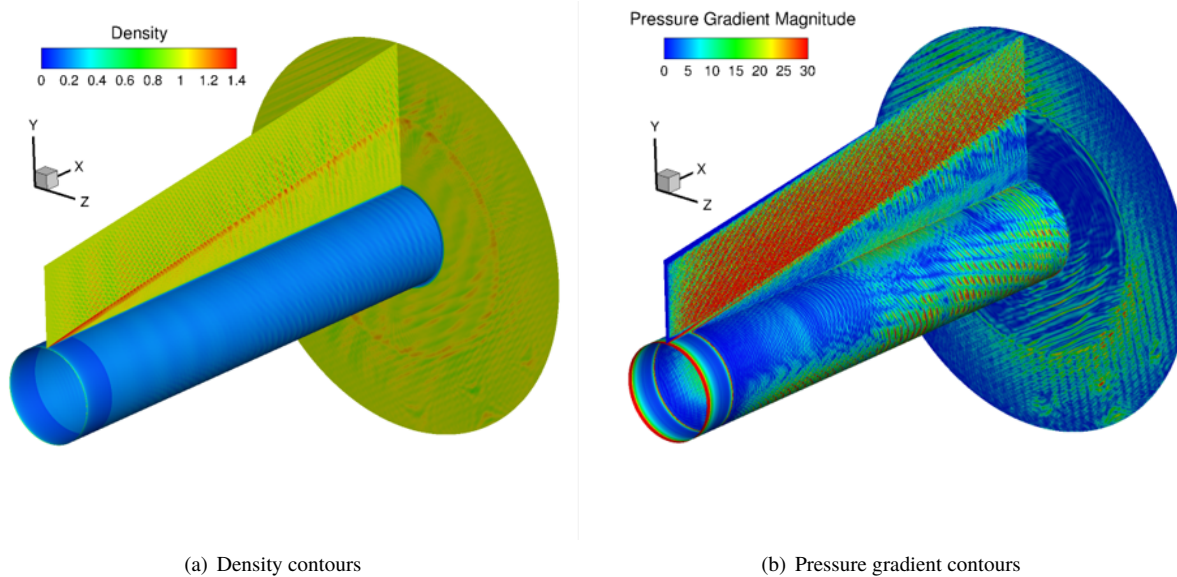

(b) Pressure gradient contours

Fig. 16   Simulation of Stetson et al. [16]'s cylinder subject to freestream acoustic forcing.

In the above images, several salient features of the flow are visible - namely, the junction between the uncooled nose tip and the constant temperature walls of each model, the development of an instability wavepacket (particularly evident in the pressure gradient contours), and the streamwise development of these instabilities as they propagate downstream. These contour plots clearly show that the freestream noise generated upstream by the curvefit model has been processed by the leading shock/Mach wave structure of each geometry and absorbed by each boundary layer. As the instabilities propagate downstream, they are modulated by the boundary layer and significant nonlinearity begins to appear.

VII. Conclusion

Linear stability theory and direct numerical simulation have been used to study the effect of acoustic noise on hypersonic laminar-turbulent boundary layer transition. LST has been used to study the disturbance frequencies which are most unstable for each geometry and to examine the effect of receptivity when the boundary layer is subjected to a tunnel noise profile representative of AEDC-VKF Tunnel B. The LST results show agreement with the data collected by Stetson et al. [16] on second mode instabilities; notably, they also indicate a difference in the receptivity process between the cylindrical and conical boundary layer. More detailed work has begun using an in-house DNS code to study the receptivity of hypersonic boundary layers to freestream forcing and the subsequent growth of instabilities. Future work will focus on refining the DNS methods used and studying the components of the downstream flowfield using Fourier decomposition to gain a better understanding of the receptivity differences between cylindrical and conical boundary layers at hypersonic velocities.

Acknowledgments

References

[1] Kovasznay, L. S., "Turbulence in supersonic flow," *Journal of the Aeronautical Sciences*, Vol. 20, No. 10, 1953, pp. 657–674.

[2] Morkovin, M. V., "On transition experiments at moderate supersonic speeds," *Journal of the Aeronautical Sciences*, Vol. 24, No. 7, 1957, pp. 480–486.

[3] Laufer, J., "Aerodynamic noise in supersonic wind tunnels," *Journal of the Aerospace Sciences*, Vol. 28, No. 9, 1961, pp. 685–692.

[4] Laufer, J., "Some statistical properties of the pressure field radiated by a turbulent boundary layer," *The Physics of Fluids*, Vol. 7, No. 8, 1964, pp. 1191–1197.

[5] Pate, S. R., and Schueler, C., "Radiated aerodynamic noise effects on boundary-layer transition in supersonic and hypersonic wind tunnels." *AIAA Journal*, Vol. 7, No. 3, 1969, pp. 450–457.

[6] Stainback, P. C., "Hypersonic boundary-layer transition in the presence of wind-tunnel noise." *AIAA Journal*, Vol. 9, No. 12, 1971, pp. 2475–2476.

[7] Kendall, J., "Wind Tunnel Experiments Relating to Supersonic and Hypersonic Boundary-Layer Transition," *AIAA Journal*, Vol. 13, No. 3, 1975, pp. 290–299. https://doi.org/10.2514/3.49694.

[8] Pate, S. R., "Dominance of Radiated Aerodynamic Noise on Boundary-Layer Transition in Supersonic-Hypersonic Wind Tunnels - Theory and Application," Arnold Engineering Development Center Report Number AEDC-TR-77-107, 1978.

[9] Schneider, S. P., "Effects of High-Speed Tunnel Noise on Laminar-Turbulent Transition," *Journal of Spacecraft and Rockets*, Vol. 38, No. 3, 2001, pp. 323–333. https://doi.org/10.2514/2.3705.

[10] Marineau, E. C., Grossir, G., Wagner, A., Leinemann, M., Radespiel, R., Tanno, H., Chynoweth, B. C., Schneider, S. P., Wagnild, R. M., and Casper, K. M., "Analysis of Second-Mode Amplitudes on Sharp Cones in Hypersonic Wind Tunnels," *Journal of Spacecraft and Rockets*, Vol. 56, No. 2, 2019, pp. 307–318.

[11] Battin, R., and Lin, C., "On the Stability of the Boundary Layer over a Cone," *Journal of the Aeronautical Sciences*, Vol. 17, No. 7, 1950, pp. 453–454.

[12] Tetervin, N., "A discussion of cone and flat-plate Reynolds numbers for equal ratios of the laminar shear to the shear caused by small velocity fluctuations in a laminar boundary layer," Tech. Rep. NACA TN 4078, National Advisory Committee on Aeronautics, 1957.

[13] Leith Potter, J., and D. Whitfield, J., "Effects of slight nose bluntness and roughness on boundary-layer transition in supersonic flows," *Journal of Fluid Mechanics*, Vol. 12, 1962, pp. 501 – 535.

[14] Pate, S. R., "Measurements and Correlations of Transition Reynolds Numbers on Sharp Slender Cones at High Speeds," *AIAA Journal*, Vol. 9, No. 6, 1971, pp. 1082–1090. https://doi.org/doi:10.2514/6.1970-799.

[15] Mack, L., "Linear Stability Theory and the Problem of Supersonic Boundary- Layer Transition," *AIAA Journal*, Vol. 13, No. 3, 1975, pp. 278–289. https://doi.org/10.2514/3.49693.

[16] Stetson, K., Kimmel, R., Donaldson, J., and Siler, L., "A comparison of planar and conical boundary layer stability and transition at a Mach number of 8," AIAA Paper 1991-1639, 1991. https://doi.org/10.2514/6.1991-1639.

[17] Chen, F., Malik, M., and Beckwith, I., "Boundary-layer transition on a cone and flat plate at Mach 3.5," *AIAA Journal*, Vol. 27, No. 6, 1989, pp. 687–693.

[18] Zhong, X., and Ma, Y., "Numerical Simulation of Leading Edge Receptivity of Stetson's Mach 8 Blunt Cone Stability Experiments," AIAA Paper 2003-1133, 2003. https://doi.org/10.2514/6.2003-1133.

[19] Ma, Y., and Zhong, X., "Receptivity of a supersonic boundary layer over a flat plate. Part 1. Wave structures and interactions," *Journal of Fluid Mechanics*, Vol. 488, 2003, p. 31–78. https://doi.org/10.1017/S0022112003004786.

[20] Ma, Y., and Zhong, X., "Receptivity of a supersonic boundary layer over a flat plate. Part 2. Receptivity to free-stream sound," *Journal of Fluid Mechanics*, Vol. 488, 2003, pp. 79–121.

[21] Balakumar, P., "Receptivity of a supersonic boundary layer to acoustic disturbances," *AIAA Journal*, Vol. 47, No. 5, 2009, pp. 1069–1078.

[22] Cerminara, A., Durant, A., André, T., Sandham, N. D., and Taylor, N. J., "Receptivity to Freestream Acoustic Noise in Hypersonic Flow over a Generic Forebody," *Journal of Spacecraft and Rockets*, Vol. 56, No. 2, 2018, pp. 447–457.

[23] Mills, M., "Hypersonic Test Capabilities in Tunnels B and C at AEDC's von Karman Facility," AIAA Paper 2015-1336, 2015.

[24] Donaldson, J., and Coulter, S., "A Review of Free-Stream Flow Fluctuation and Steady-State Flow Quality Measurements in the AEDC/VKF Supersonic Tunnel A and Hypersonic Tunnel B," AIAA Paper 95-6137, 1995.

[25] Marineau, E. C., "Prediction methodology for second-mode-dominated boundary-layer transition in wind tunnels," *AIAA Journal*, Vol. 55, No. 2, 2016, pp. 484–499.

[26] Duan, L., Choudhari, M. M., Chou, A., Munoz, F., Radespiel, R., Schilden, T., Schröder, W., Marineau, E. C., Casper, K. M., Chaudhry, R. S., et al., "Characterization of freestream disturbances in conventional hypersonic wind tunnels," *Journal of Spacecraft and Rockets*, Vol. 56, No. 2, 2019, pp. 357–368.

[27] Pinna, F., "VESTA toolkit: A software to compute transition and stability of boundary layers," *43rd AIAA Fluid Dynamics Conference*, 2013, p. 2616.

[28] Trefethen, L. N., *Spectral methods in MATLAB*, Vol. 10, Society for Industrial and Applied Mathematics, 2000.

[29] Groot, K. J., Miró Miró, F., Beyak, E. S., Moyes, A., Pinna, F., and Reed, H. L., "DEKAF: spectral multi-regime basic-state solver for boundary layer stability," AIAA Paper 2018-3380, 2018.

[30] van Ingen, J., "A suggested semi-empirical method for the calculation of the boundary layer transition region," Tech. Rep. VTH-74, Technische Hogeschool Delft, Vliegtuigbouwkunde, 1956.

[31] van Ingen, J., "The e^N method for transition prediction. Historical review of work at TU Delft," AIAA Paper 2008-3830, 2008.

[32] Poggie, J., "High-Order Compact Difference Methods for Glow Discharge Modeling," AIAA Paper 2009-1047, 2009.

[33] Poggie, J., Adamovich, I., Bisek, N., and Nishihara, M., "Numerical simulation of nanosecond-pulse electrical discharges," *Plasma Sources Science and Technology*, Vol. 22, No. 1, 2012, p. 015001.

[34] Poggie, J., Bisek, N. J., Leger, T., and Tang, R., "Implicit Large-Eddy Simulation of a Supersonic Turbulent Boundary Layer : Code Comparison," AIAA Paper 2014-0423, 2014.

[35] Poggie, J., "Large-Scale Structures in Implicit Large-Eddy Simulation of Compressible Turbulent Flow," *7th AIAA Theoretical Fluid Mechanics Conference*, 2014, p. 3328.

[36] Poggie, J., Bisek, N. J., and Gosse, R., "Resolution effects in compressible, turbulent boundary layer simulations," *Computers & Fluids*, Vol. 120, 2015, pp. 57–69.

[37] Beam, R. M., and Warming, R. F., "An implicit finite-difference algorithm for hyperbolic systems in conservation-law form," *Journal of Computational Physics*, Vol. 22, No. 1, 1976, pp. 87–110.

[38] Pulliam, T. H., and Chaussee, D., "A diagonal form of an implicit approximate-factorization algorithm," *Journal of Computational Physics*, Vol. 39, No. 2, 1981, pp. 347–363.

[39] Garmann, D. J., "Characterization of the vortex formation and evolution about a revolving wing using high-fidelity simulation," Ph.D. thesis, University of Cincinnati, 2013.

[40] Gaitonde, D., Shang, J., and Young, J., "Practical aspects of high-order accurate finite-volume schemes for electromagnetics," AIAA Paper 97-036, 1997.

[41] Tufts, M. W., Bisek, N. J., and Kimmel, R. L., "Implicit Large-Eddy Simulation of Discrete Roughness Boundary-Layer Transition with Added Perturbations," AIAA Paper 2019-2967, 2019.